Universal statistics of nanocrystal photoluminescence

Leo Luber[1], Daphne Benedikt[1], Andreas Singldinger[1], and Alexander S. Urban[1,*]

[1]Nanospectroscopy Group and Center for NanoScience, Faculty of Physics, Ludwig-Maximilians-Universität München, Königinstr. 10, 80539 München, Germany
[*]Correspondence to: urban@lmu.de

January 14, 2026

Supplementary Note 1 Detecting nanocrystal (NC) polydispersity from photoluminescence (PL) spectra through lineshape fits

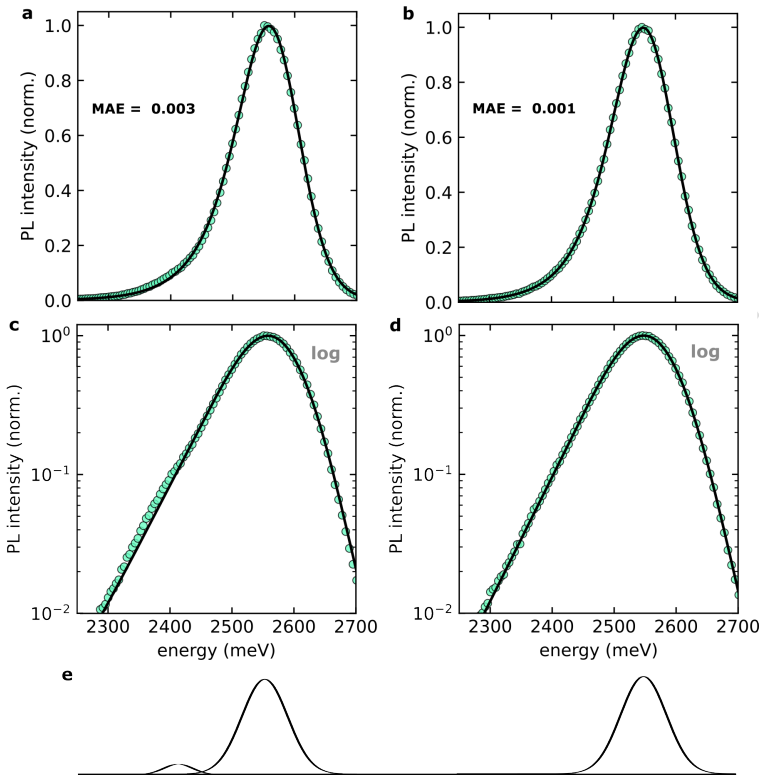

Supplementary Fig. 1: Detection of hidden subpopulations from ensemble PL spectra. a,b, Representative PL spectra of two $CsPbBr_3$ nanocube ensembles with similar mean size but differing purity. While both spectra appear nearly identical on a linear scale, the mixed sample (a) contains a small subpopulation of larger cubes, producing a shoulder in the ensemble distribution. **c,d**, Corresponding logarithmic plots highlight the deviation of the experimental data (symbols) from the fitted GaLa profile (lines). The mean absolute error (MAE) increases from 0.001 for the pure sample to 0.003 for the mixed one, demonstrating that even weak secondary populations can be quantitatively detected through the residuals of the GaLa fit. **e**, Schematic (exaggerated) visualization of the bimodal and unimodal Gaussian components of the two samples.

Supplementary Note 2 Comparsion of on-film and dispersion PL measurements

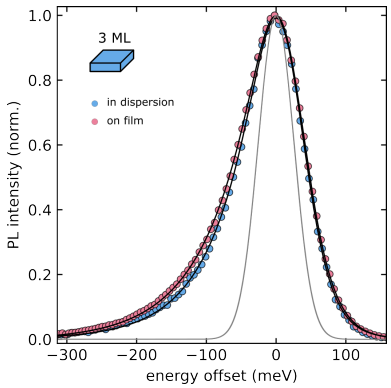

Supplementary Fig. 2: Comparison of on-film and dispersion PL measurements of an exemplary 3ML nanoplatelet sample. The film sample was prepared by dropcasting 100 μl of the undiluted synthesis product on a 10 mm x 10 mm silicon oxide substrate and the PL measurement was conducted with the same FluoroMax-4Plus spectrometer (HORIBA Scientific) setup (Methods). Between the two environments both σ and the high energy tail w_h remain invariant. The low-energy tail is affected by on-film dynamics causing an small increase of w_l from 61 meV to 69 meV.

Supplementary Note 3 Excitation-dependence

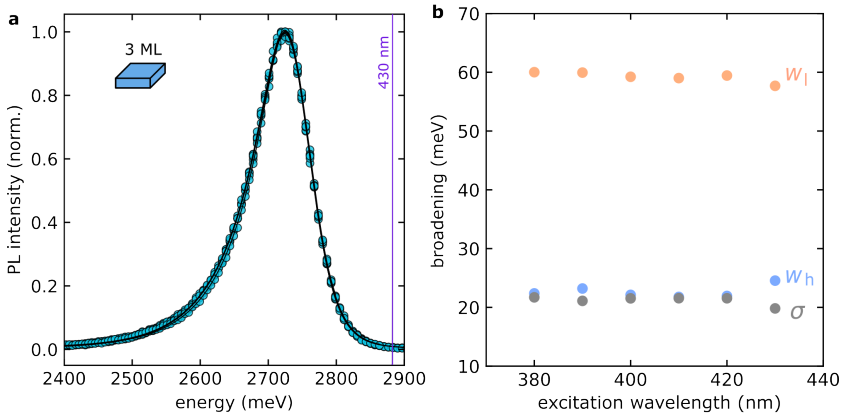

Supplementary Fig. 3: Excitation-wavelength independence of the photoluminescence lineshape. **a**, Representative normalized PL spectra of a 3ML $CsPbBr_3$ nanoplatelet ensemble measured at different excitation wavelengths λ_{exc} between 380 and 430 nm. All spectra are identical within experimental noise. **b**, Extracted parameters σ, w_h (high-energy tail width), and w_l (low-energy tail width) show no dependence on excitation wavelength. The excitation-invariant behavior confirms that the PL lineshape and its fitted parameters are intrinsic to the thermalized exciton ensemble and unaffected by excitation energy. (This is not necessarily the case for excitations within the emission range of the NC ensemble.)

Supplementary Note 4 Controlling low-energy emission in 2D NCs through surface treatment

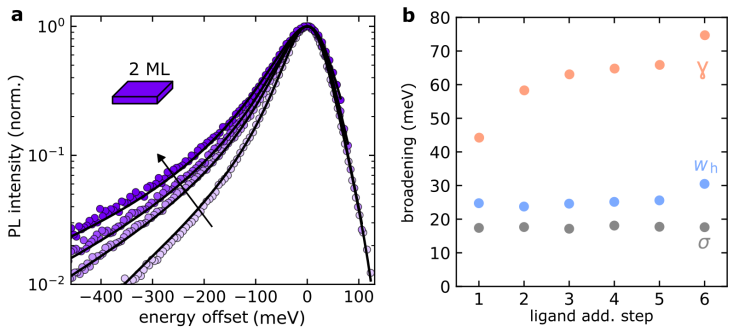

Supplementary Fig. 4: Evidence for a surface-dependence of the Lorentzian distributed low-energy tail. **a**, An initial $CsPbBr_3$ 2ML nanoplatelet sample was treated with 0, 5, 10, 20, 30, and 50 μl of OD-PEA[1] ligand solution in toluene (10 mg/mL) (bright to dark) for which 4 exemplary PL spectra (0, 10, 30, and 50) and GaLx fits are shown. **b**, Both fitting parameters w_h and σ show a stable level throughout the treatment while γ nearly doubles. The change in ligand passivation is assumed to change the exciton–phonon coupling in 2ML nanoplatelets as suggested by Tao et al.[2] and resolved here by the change in Lorentzian tail width.

Supplementary Note 5 $\sigma(T)$ between 4 K and 300 K

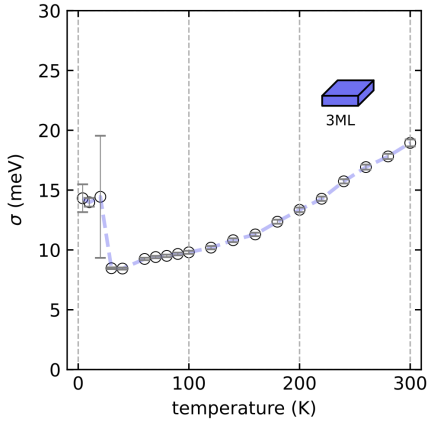

Supplementary Fig. 5: Tracing σ from 4 K to 300 K. For the 3ML nanoplatelet thin-film sample the Gaussian PL component σ is evaluated from a GaLa fit. Between the limits of the temperature range we find a similar Gaussian broadening, while the intermediate regime exhibits some non-trivial behavior. The room temperature extracted Gaussian broadening acts as an upper bound on $\sigma(T)$ for all spectra.

Supplementary Note 6 Evaluating size dispersion from non-ABX_3 QD ensemble PL

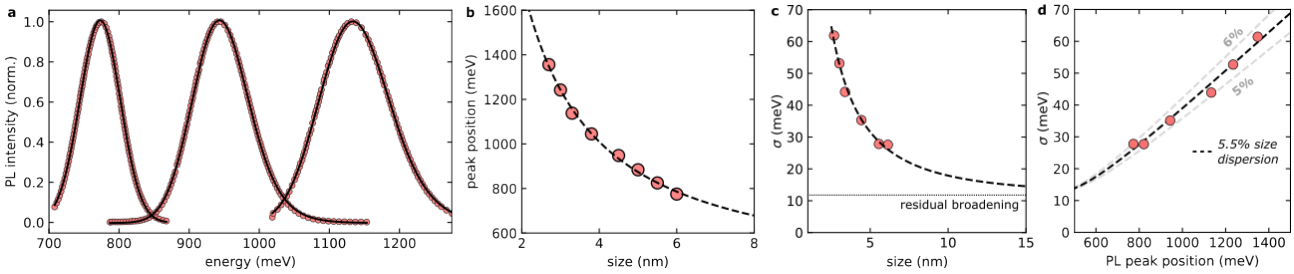

Supplementary Fig. 6: Evaluating size dispersion of PbS QDs by *Quantum Solutions*. **a**, A selection of PL spectra (data extracted from published figures)[3] is shown together with GALa lineshape fits. **b**, The provided information about mean sizes is used to (re)construct a sizing curve for the material. The offset $E_0 = (0.40 \pm 0.13)$ eV shows great agreement with the band gap of 0.42 eV[4] confirming the validity of this approach. **c**, For samples with a fitting error MAE< 0.005 the Gaussian broadening is evaluated and follows the expected trend across a range of NC sizes with the familiar concept of a residual broadening in the unconfined limit. **d**, All samples are found to roughly follow a line of constant size dispersion around 5 - 6 % which agrees with the published upper bound of $<$ 5-10 %.

Supplementary Note 7 The influence of NC anisotropy on inhomogeneous broadening

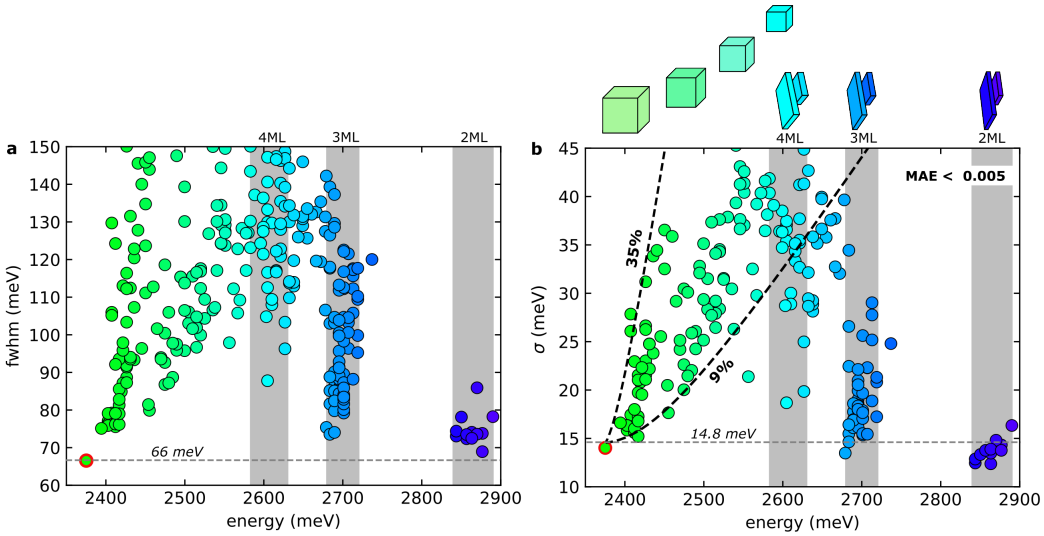

Supplementary Fig. 7: Reduction of size dispersion through NC anisotropy and the morphology-independence of σ_0. **a**, The full width at half maximum (FWHM) data is shown for the entire dataset from Henke et al. relative to the established population boundaries[5] of nanoplatelets with the additional nanocube sample produced by this work (red cirlcle). **b**, For the same samples GaLa and GaLx lineshape fits were used to evaluate σ, while all datapoints with a fitting error (MAE) > 0.005 were excluded to remove polydisperse ensembles. $\sigma_0 = 14.8$ meV for nanocubes is shown and shows good agreement with the largest 3ML nanoplatelets as well as most 2ML nanoplatelets. The latter almost always far exceed the exciton Bohr diameter in lateral size while the thickness should exhibit no size dispersion in a monodisperse nanoplatelet sample. This way, large nanoplatelets of any number of monolayers should always approach the residual inhomogeneous broadening. The observation that this limit σ_0 is seemingly independent of the NC morphology or anisotropy, is non-trivial and hints at a fundamental material parameter. This discussion also empathizes the extraordinary importance of developing (ambient condition) approaches to pure nanoplatelet samples with > 3 monolayers to close the gap in super-narrow emitters between 2400 meV and 2700 meV. While 4-6 ML emitters were presented in a select few publications[5,6], FWHM values close to or even below 70 meV (indicating true monodispersity) have to our knowledge not been achieved and are the target of ongoing research. The narrow outlier around 2560 meV was characterized as an ensemble of anisotropic shapes and therefore excluded from the main dataset in this work.

Supplementary Note 8 Unconfined NCs from extreme dilution synthesis

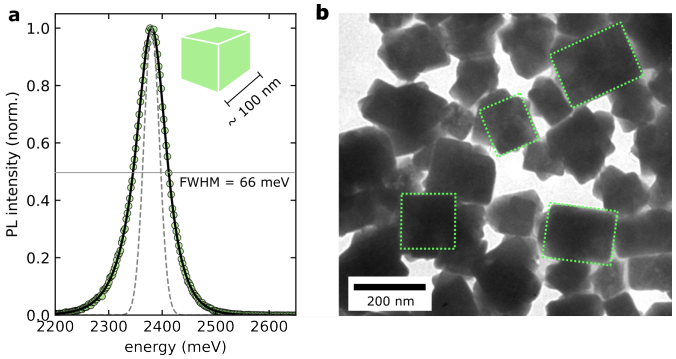

Supplementary Fig. 8: A $CsPbBr_3$ NC population with mean dimensions ≈ 100 nm in the unconfined regime. The sample was produced with a novel, highly diluted synthesis protocol allowing for unconstrained NC growth. **a**, A PL spectrum with the record 300 K FWHM value of 66 meV with a GaLa fit and **b**, a transmission electron microscopy (TEM) image.

Supplementary Note 9 Size dispersion and tail statistics analysis for published PL data

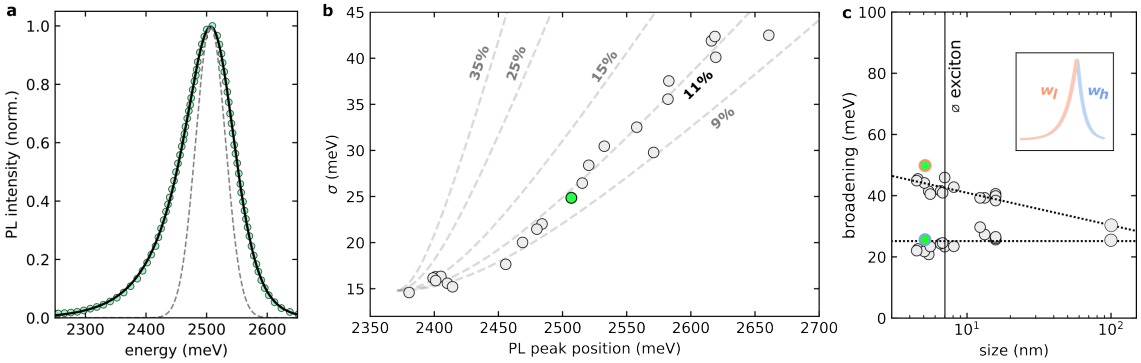

Supplementary Fig. 9: Unbiased testing of the presented PL analysis methodology on published PL data. **a**, A PL spectrum of a $CsPbBr_3$ nanocube ensemble with mean size of 5 nm extracted from a published figure by Boehme et al.[7]. **b**, The evaluated PL peak position and Gaussian broadening σ places it close to the 9-10 % upper bound reported by the authors. **c**, Similarly, both evaluated tail widths also closely follow the size dependent trends resolved in Fig. 4e showing an overall consistency of the framework with unbiased test data. (Note that the same residual floor σ_0 is assumed although the instrument broadening contribution could be slightly different for this PL measurement.)

Supplementary Note 10 Lineshape evolution under ion exchange

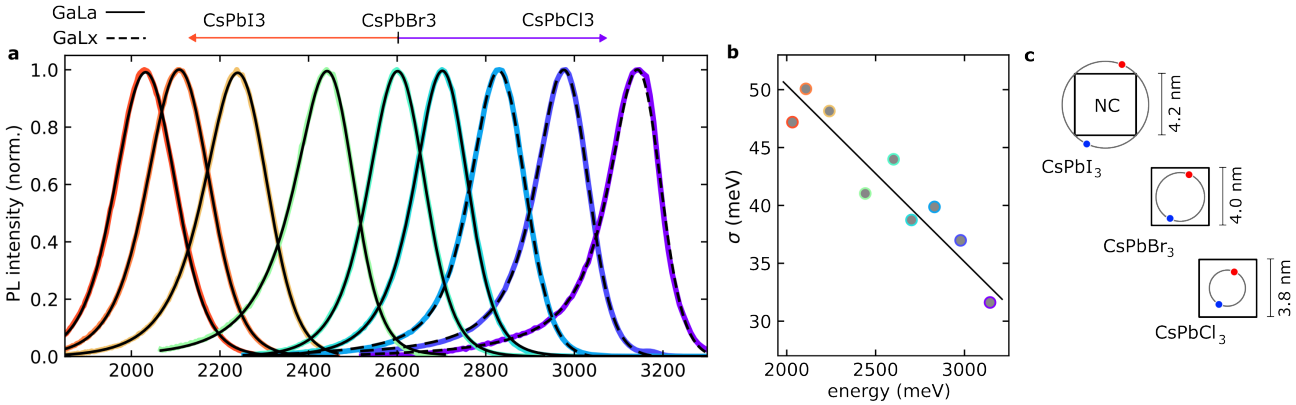

Supplementary Fig. 10: Linear scaling of inhomogeneous broadening with emission energy across halide compositions. **a**, PL spectra of halide-exchanged $CsPbX_3$ nanocubes (X = I, Br, Cl) spanning the visible to near-infrared range taken from Abfalterer et al.[8] with GaLa/GaLx lineshape fits. The later model was chosen for the $CsPbCl_3$ compositions as they showed better agreement with the low-energy tails in this particular case. **b**, Extracted Gaussian widths σ plotted versus emission energy show a strong correlation (black line as a guide for the eye). **c**, Schematic illustration of exciton Bohr radii[9] for the three halide compositions, highlighting the increasing confinement with smaller halide ions. The observed connection between σ and Bohr radius demonstrates that the Gaussian width reflects intrinsic excitonic confinement and dielectric screening effects, further supporting its physical interpretation as inhomogeneous broadening arising from energetic disorder.

Supplementary Note 11 Well-behaved optimization of the GaLa lineshape function

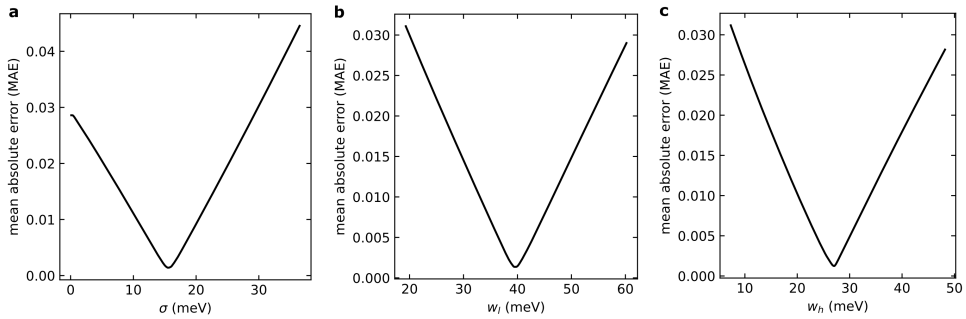

Supplementary Fig. 11: Behaviour of the fitting MAE under parameter variation. The PL spectrum from Fig. 1e is used as an example. **a-c**, The evolution of the fitting error under variation of a single fitting parameter (w_h, w_l, or σ) is evaluated while keeping the other values constant at the optimal value. Both the "sharp" global minimum as well as the steep gradients around it suggest a well behaved optimization problem with a precisely defined solution. For a high quality PL spectrum there is no ambiguity in the GaLa lineshape parameters.

Supplementary Note 12 Validation of the sizing-curve on published data

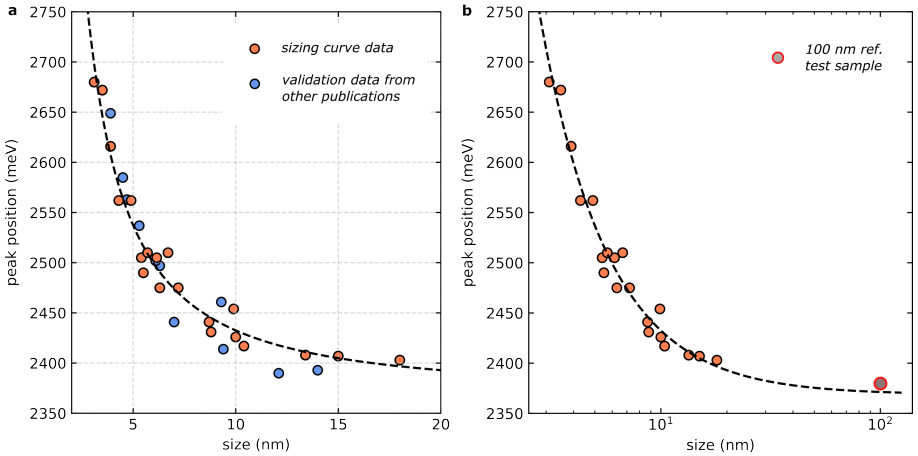

Supplementary Fig. 12: Comparing the implemented sizing-curve to established test data. **a**, To test the generality of our $CsPbBr_3$ NC sizing curve we overlay the data and power-law model with independent published data[10–13]. We find decent agreement and therefore conclude that our mapping is largely unbiased and resembles a good estimation of NC confinement energies. **b**, Additionally, we find excellent agreement between the PL peak prediction of the sizing curve model with our 100 nm cube population (Methods).

Supplementary Note 13 Estimating size-dependent inhomogeneous broadening from TEM images

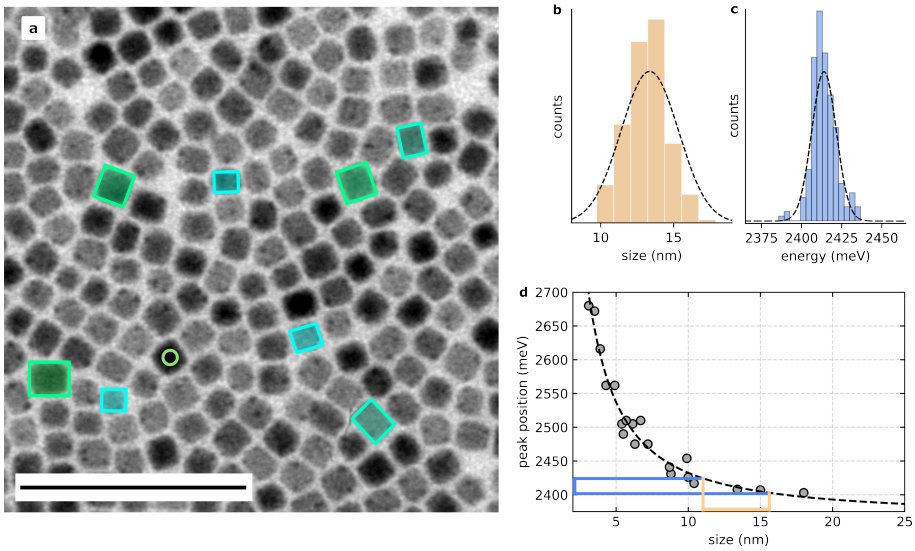

Supplementary Fig. 13: Pipeline for estimating excitonic gap distributions from TEM images. **a**, An exemplary TEM image of a $CsPbBr_3$ nanocube ensemble with a scale bar of 100 nm (black line) and the expected exciton diameter (green circle). **b**, A histogram resulting from ≥ 100 evaluated NC dimensions with a Gaussian fit (dotted line). **c**, Each NC size is then translated into the energy domain by **d**, the established sizing curve (Methods). The transformation from a distribution over sizes (orange) to a distribution over energy (blue) with σ according to Eq. (5) is illustrated. Note the strong dependence of the linewidth in energy on the gradient of the sizing curve at the relevant region. A convolution with the residual floor σ_0 and the thermal tails then generates the estimated PL lineshape. While this method generally reproduces the spectra shape with very high accuracy, the predicted peak position is often shifted by a few meV due to the error of the sizing curve predictor. This offset was adjusted afterwards to better demonstrate the agreement between PL statistics and lineshape prediction.

Removing sources of bias. It is critical to ensure that the evaluated TEM images resemble the true size distribution in the NC sample and that no step in the evaluation process is biased towards particular sizes. The analysis was performed on many distinct regions on on the TEM grid and from several images. For randomly chosen spots all NCs within a that particular region were measured along an arbitrary crystal axis.

Potential de-convolution of the TEM evaluation error. As TEM size evaluations are not perfect, the evaluated size distribution $\sigma_{L,measured}$ carries contributions from the true size dispersion $\sigma_{L,true}$ as well as the measurement error $\sigma_{L,err}$ of every single NC. Under the assumption of independent variables, the true standard deviation would then be given by $\sigma_{L,true} = \sqrt{\sigma^2_{L,measured} - \sigma^2_{L,err}}$. While such a step was not implemented in this work, to achieve the full potential of the presented methodology in future applications, this adjustment should be considered. The ratio between $\sigma_{L,true}$ and $\sigma_{L,err}$ is quite significant here. For low quality TEM images the evaluation error can approach the standard deviation of the true size dispersion, where the measurement error overshadows the distribution one wants to resolve. This generally sets requirements on the quality of TEM images used in this context.

Monte-Carlo error propagation. To estimate the error in the final σ we perform a Monte-Carlo error propagation, sampling from a Gaussian distribution for each error contribution. Here we consider the sampling error, the leave-one-out error of the sizing curve as an emission energy predictor evaluated as 20 meV and the error in the residual Gaussian broadening σ_0. The latter is taken from Fig. 4c as 0.5 meV. By running the Monte-Carlo simulation for 10000 iterations we obtain a final distribution of occurring values for σ from which we evaluate the corresponding standard deviation. The resulting error bars are not intrinsic to the method presented here and can be reduced by increasing the number of size measurements or the accuracy of the sizing-curve.

Advantages of GaLa PL fits and σ as a measure of sample homogeneity compared to TEM imaging. Considering the previously mentioned limitations, extracting sample purity and size dispersions from TEM images is prone to evaluation biases and generally results in significant error bars. In contrast, the GaLa fitting parameters

represent an unbiased, robust average across the NC ensemble with errors on the order of 0.1 meV and require a much less time intensive measurement process. We therefore conclude, that σ and the GaLa framework overall represent a more reliable and highly efficient evaluation of sample homogeneity.

Supplementary Note 14 Comparing Voigt, GaLa, and GaLx fitting functions

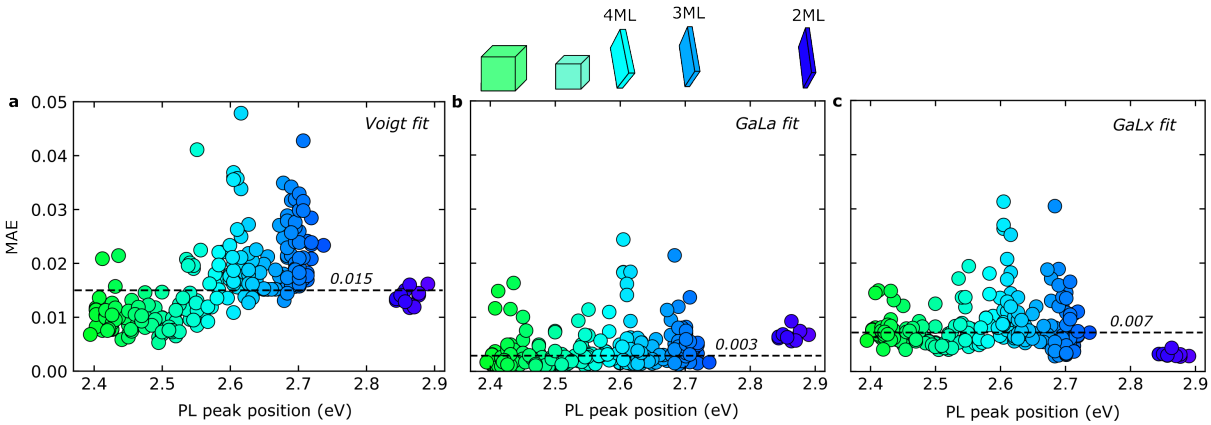

Supplementary Fig. 14: Testing fitting functions on the Henke et al. dataset[5]. The spectra were selected according to the monodispersity label taken from Henke et al. and the MAE fitting error was evaluated for: **a**, the conventional Voigt fit, as well as the two lineshapes introduced by this work: the GaLa function (**b**) and the GaLx function (**c**). The median errors across all samples are marked. The outliers here are caused by minor impurities that were not accounted for in the original publication instead of a fundamental deviation. Both novel approaches far outperform the Voigt fit and show exceptional agreement in their respective regime: GaLx in the 2D limit, GaLa for all other populations.

Supplementary Note 15 GaLa line shape reproduces electroluminescent spectra

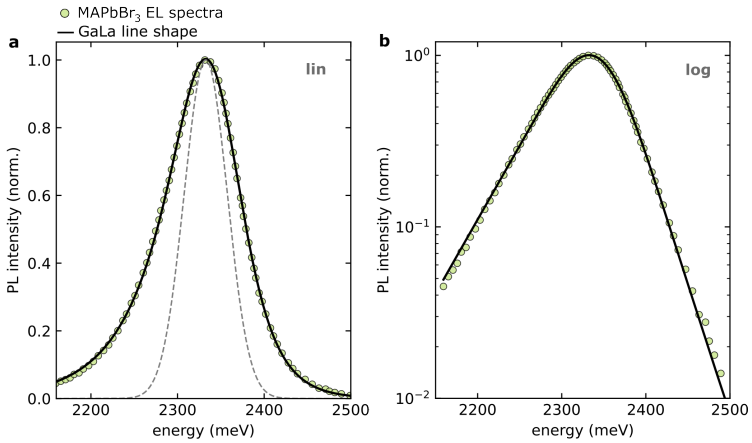

Supplementary Fig. 15: $MAPbBr_3$ electroluminescence (EL) spectra follow GaLa statistics. For an exemplary EL spectrum extracted from a published figure in Leyden et al.[14] the agreement between data and fitting function is decent both on the linear (**a**) and logarithmic scale (**b**). The minimal deviations are likely a consequence of the data extraction method.

References

1. Morad, V., Stelmakh, A., Svyrydenko, M. et al. Designer phospholipid capping ligands for soft metal halide nanocrystals. *Nature* **626,** 542–548 (2024).
2. Tao, W., Zhang, C., Zhou, Q., Zhao, Y. & Zhu, H. Momentarily trapped exciton polaron in two-dimensional lead halide perovskites. *Nat. Commun.* **12** (2021).
3. QDot™ PbS quantum dots. *Quantum Solutions* https://quantum-solutions.com/product/qdot-lead-sulfide-pbs-quantum-dots/#technical (2025).
4. Cho, B., Peters, W. K., Hill, R. J., Courtney, T. L. & Jonas, D. M. Bulklike hot carrier dynamics in lead sulfide quantum dots. *Nano Lett.* **10,** 2498–2505 (2010).
5. Henke, N. A. et al. Synthesizer: machine learning-guided perovskite nanocrystal optimization. *Adv. Mater.* (2025).
6. Bertolotti, F. et al. Crystal structure, morphology, and surface termination of cyan-emissive, six-monolayers-thick $CsPbBr_3$ nanoplatelets from x-ray total scattering. *ACS Nano* **13,** 14294–14307 (2019).
7. Boehme, S. C. et al. Strongly confined $CsPbBr_3$ quantum dots as quantum emitters and building blocks for rhombic superlattices. *ACS Nano* **17,** 2089–2100 (2023).
8. Abfalterer, A. et al. Room-temperature synthesis of strongly confined lead halide perovskite quantum dots. Preprint at chemrxiv (2026).
9. Protesescu, L. et al. Nanocrystals of cesium lead halide perovskites ($CsPbX_3$, X = Cl, Br, and I): novel optoelectronic materials showing bright emission with wide color gamut. *Nano Lett.* **15,** 3692–3696 (2015).
10. Kline, J. et al. Emissive traps lead to asymmetric photoluminescence line shape in spheroidal $CsPbBr_3$ quantum dots. *Nano Lett.* **25,** 5063–5070 (2025).
11. Raino, G. et al. Ultra-narrow room-temperature emission from single $CsPbBr_3$ perovskite quantum dots. *Nat. Commun.* **13,** 2587 (2022).
12. Li, J. et al. Temperature-dependent photoluminescence of inorganic perovskite nanocrystal films. *RSC Adv.* **6,** 78311–78316 (2016).
13. Cheng, O. H.-C., Qiao, T., Sheldon, M. & Son, D. H. Size- and temperature-dependent photoluminescence spectra of strongly confined $CsPbBr_3$ quantum dots. *Nanoscale* **12,** 13113–13118 (2020).
14. Leyden, M. R. et al. Methylammonium lead bromide perovskite light-emitting diodes by chemical vapor deposition. *J. Phys. Chem. Lett.* **8,** 3193–3198 (2017).